doi:10.1016/j.jmb.2012.02.016 J. Mol. Biol. (2012) 418, 117–126

Contents lists available at www.sciencedirect.com

Journal of Molecular Biology

journal homepage: http://ees.elsevier.com.jmb

Projection Structure of the Secondary Citrate/Sodium Symporter CitS at 6 Å Resolution by Electron Crystallography

Fabian Kebbel[1]†, Mareike Kurz[2]†, Markus G. Grütter[2]* and Henning Stahlberg[1]*

[1]*Center for Cellular Imaging and NanoAnalytics (C-CINA), Biozentrum, University Basel, Mattenstrasse 26, CH-4058 Basel, Switzerland*
[2]*Department of Biochemistry, University Zürich, Winterthurerstrasse 190, CH-8057 Zürich, Switzerland*

Received 20 December 2011; received in revised form 3 February 2012; accepted 11 February 2012
Available online 17 February 2012

Edited by J. Bowie

Keywords:
secondary transporter;
2-hydroxycarboxylate transporter (2-HCT);
CitS;
electron crystallography;
cryo-electron microscopy

CitS from *Klebsiella pneumoniae* acts as a secondary symporter of citrate and sodium ions across the inner membrane of the host. The protein is the best characterized member of the 2-hydroxycarboxylate transporter family, while no experimental structural information at sub-nanometer resolution is available on this class of membrane proteins. Here, we applied electron crystallography to two-dimensional crystals of CitS. Carbon-film-adsorbed tubular two-dimensional crystals were studied by cryo-electron microscopy, producing the 6-Å-resolution projection structure of the membrane-embedded protein. In the $p22_12_1$-symmetrized projection map, the predicted dimeric structure is clearly visible. Each monomeric unit can tentatively be interpreted as being composed of 11 transmembrane α-helices. In projection, CitS shows a high degree of structural similarity to NhaP1, the Na^+/H^+ antiporter of *Methanococcus jannaschii*. We discuss possible locations for the dimer interface and models for the helical arrangements and domain organizations of the symporter based on existing models.

Introduction

Two different membrane protein classification schemes were established during the last decades. The classical transporter classification system[1] is based on the function (mode of transport) and molecular phylogeny of transport proteins. According to the transporter classification system, more than 250 putative transport protein families have been identified.[1–3] A more recent classification system (MemGen), developed by Lolkema and Slotboom,[4,5] groups membrane proteins into structural classes based on their hydropathy profile that is proposed to represent a specific fold. According to the MemGen classification system, structural class ST[3] contains several thousands of different secondary transporters from 32 families.[6] In both systems, secondary transporters represent one of the largest functional categories. These transporters exploit energy stored in ion and/or solute gradients across the membrane to drive substrate transport and are generally classed in three groups regarding their mode of energy coupling, that is, symporters, antiporters, and uniporters.[7] Secondary transporters

**Corresponding authors.* H. Stahlberg is to be contacted at Center for Cellular Imaging and NanoAnalytics (C-CINA), Biozentrum, University Basel, WRO-1058, Mattenstrasse 26, CH-4058 Basel, Switzerland.
E-mail addresses: Gruetter@bioc.unizh.ch; Henning.Stahlberg@unibas.ch.
† These authors contributed equally.

Abbreviations used: 2D/3D, two-/three-dimensional; 2-HCT, 2-hydroxycarboxylate transporter; DM, *n*-decyl-β-D-maltoside; EM, electron microscopy; LPR, lipid-to-protein ratio; TMS, transmembrane segment.

are ubiquitously spread across all kingdoms of life and their abundance is reflected in the vast diversity of encoded sequences.

Major efforts in biomolecular structure determination over the last decades led to an increasing number of three-dimensional (3D) crystal structures of secondary transporters. Among others, these are AcrB,[8] LacY,[9] GlpT,[10] NhaA,[11] ClC,[12] Glt_{Ph},[13] LeuT,[14] AAC1,[15] SGLT,[16] UCP2,[17] EmrD,[18] EmrE,[19–22] FucP,[23] Mhp1,[24] BetP,[25] AdiC,[26] ApcT,[27] CaiT,[28] $PepT_{So}$,[29] UraA,[30] and ASBT.[31] However, none of those belongs to the structural class ST[3] of the MemGen classification system. Interestingly, the solved structures reveal several different folds and hence several different substrate translocation mechanisms.[7,32] The structures allow a first understanding of the translocation mechanism in the many different families of secondary transporters.

One family of secondary transporters is represented by the 2-hydroxycarboxylate transporters (2-HCTs). 2-HCTs are found in the ST[3] class in the MemGen system and, being the biochemically best-studied family in this class so far, serve as a paradigm for the 31 other families.[6] A characteristic feature of the exclusively bacterial 2-HCT family is the transport of substrates containing the 2-hydroxycarboxylate motif ($HO\text{-}CR_2\text{-}COO^-$) as found in citrate, malate, or lactate.[32,33] Well-studied 2-HCT members are proton symporters (CimH of *Bacillus subtilis*, MaeP of *Streptococcus bovis*), precursor/product exchangers (CitP of *Leuconostoc mesenteroides*, MleP of *Lactococcus lactis*), and sodium symporters (CitS of *Klebsiella pneumoniae*, MaeN of *B. subtilis*).

Functionally and structurally, the Na^+/citrate symporter CitS from *K. pneumoniae* is the best-characterized 2-HCT member. Studies on CitS have resulted in a detailed topological model of this transporter as a representative for all 2-HCT members (Fig. 1a). The core structure for 2-HCTs consists of two homologous domains (N-/C-domain) connected by a large cytoplasmic loop. Each domain carries five transmembrane segments (TMSs). The two domains share a similar fold, but due to the odd number of TMSs, they have opposite orientations in the membrane (inverted topology).[32,34,35] CitS possesses one additional TMS at the N-terminus, leading to a total of 11 TMS with the NH_2- and COOH-termini at the cytoplasmic and periplasmic side of the membrane, respectively[36] (Fig. 1a). Furthermore, TMSs VIII and IX are connected *via* an intracellular amphipathic surface helix (AH).[37]

Structural and biophysical studies suggested detergent-solubilized and purified CitS to exist as an elliptical shaped homodimer.[38,39] Krupnik *et al.* assigned the interface between the two monomers to the short axis of the elongated particle, leaving the long axis for the interface between the N- and C-terminal domains within one monomer (Fig. 1b).[40] This study also suggested the N-terminal TMS to be located close to the dimer interface, while the long cytoplasmic loop was positioned to the end of the long axis. The Lolkema group identified a highly conserved arginine residue, Arg428, at the cytoplasmic end of TMS 11. It was proposed that Arg428 might be directly involved in the high-affinity binding of one carboxyl group of the bivalent citrate anion.[41] Additionally, CitS exhibits two reentrant loops Vb and Xa, which fold back in between the TMSs from opposite sides of the membrane. The tips of the loop are formed by the highly conserved

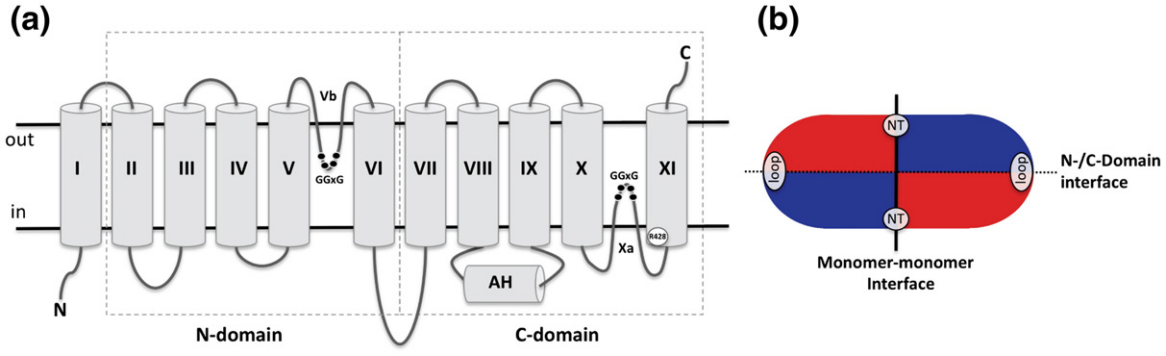

Fig. 1. Topology model and domain organization of CitS. (a) Topology model of CitS. The protein consists of 10+1 TMSs (TMSs I–XI) organized as N-terminal and C-terminal domains (5 TMSs each) with inverted topology, plus 1 single TMS. A large cytoplasmic loop connects both domains. Between the fourth and fifth TMS in each domain, a reentrant loop (Vb and Xa) folds into the membrane with the conserved GGXG motif at its tip. TMS XI carries the highly conserved Arg428, which is involved in substrate binding. (b) Model of dimer interface and domain organization. The monomer–monomer interface is formed by the short axis of the elliptical CitS dimer. The N- and C-domains (depicted in blue/red or red/blue, respectively) are separated by the long axis. The ends of both axes also house the N-terminus (NT) and the cytoplasmic loop.

GGxG sequence motif, which can be found in most of the 2-HCT members. It is hypothesized that these reentrant loops in the N- and C-domains might be in close proximity in the 3D structure at the interface of the two domains, thereby forming the translocation pathway for citrate and sodium ions.[42,43]

Functionally, it has been postulated that CitS co-transports citrate as a divalent citrate anion ($HCit^{2-}$) coupled with two Na^+ ions and one H^+ using the electrochemical gradient of Na^+.[44,45] During substrate translocation, CitS most likely exhibits two main conformational states, in which the substrate binding pocket is exposed to either the extracellular medium or the cytosol. This mechanism of "alternating access" seems to be a common feature for secondary transporters as confirmed by high-resolution 3D structures of several transporters.[46] However, the exact transport mechanisms and substrate stoichiometries in the 2-HCT transporter family are still not fully determined.

In this study, we present the first sub-nanometer resolved structural data of CitS revealed by electron crystallography of two-dimensional (2D) crystals of recombinant CitS embedded in an artificial lipid bilayer. The projection structure of the membrane-embedded protein at 6 Å resolution clearly shows a homodimeric structure with each monomer exhibiting 11 electron-dense regions likely corresponding to transmembrane α-helices. Based on this projection structure, we discuss different models for possible dimer interfaces as well as possible arrangements of the N- and C-terminal domains.

Results and Discussion

Electron crystallography

Highly pure and homogeneous recombinant CitS expressed in *Escherichia coli* was used for 2D crystallization experiments. The purity was confirmed by SDS-PAGE analysis showing one major band at ~35 kDa corresponding to monomeric CitS (Fig. 2a). A second faint band at 65 kDa indicated the presence of small amounts of dimeric CitS in SDS, documenting a weak interaction between the two monomers. Numerous crystallization parameters had to be varied over a wide range to find the most suitable conditions for highly ordered 2D crystals (Table 1). The highest impact on crystal formation and crystal order was found by varying pH, NaCl concentration, lipid-to-protein ratio (LPR), and the type of synthetic lipids. The best conditions (20 mM acetate, pH 4.5, 500 mM NaCl, 15 mM $MgCl_2$, 2 mM DTT, and 0.02% NaN_3,) led to tubular 2D crystals measuring a diameter of 0.2–0.3 μm and a length of 1–2 μm (Fig. 2b and c). The high order of the planar–tubular crystals was confirmed by the power spectrum of negatively stained crystals yielding spots to a resolution of 24 Å. Tubular crystals grew only within a very small LPR range of 0.32–0.35 (w/w). Slightly higher or lower LPRs led to wrinkled tubes or small disordered vesicles, respectively. Additionally, we found the wider planar tubes to be much better ordered than crystals with smaller diameters. Hence, CitS may have the intrinsic tendency to form tubes within a small size

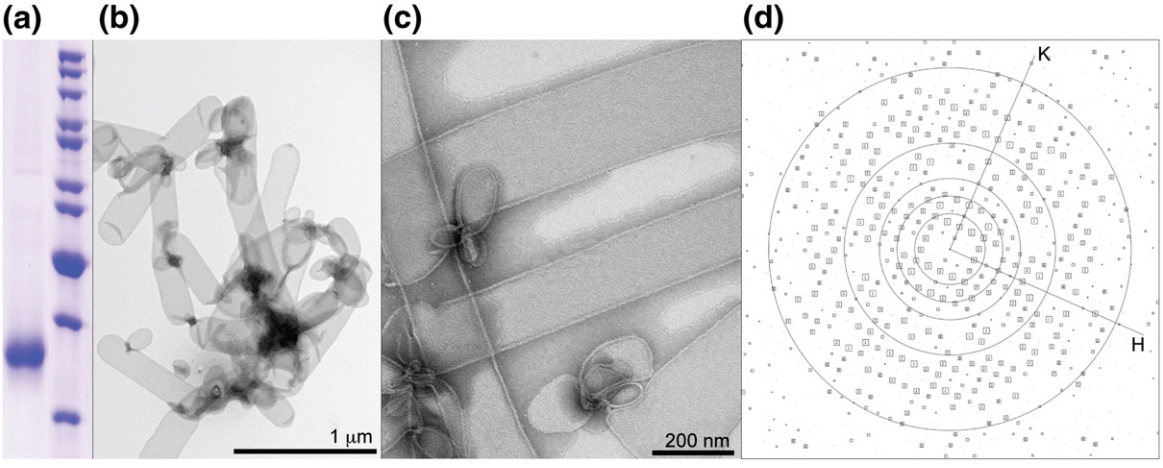

Fig. 2. Purification and 2D crystallization of CitS. (a) SDS-PAGE of purified CitS. The prominent band at 35 kDa corresponds to monomeric CitS, while a faint band at 65 kDa represents the dimer. Molecular mass marker bands are 200, 150, 120, 100, 85, 70, 60, 50, 40, and 30 kDa. (b and c) Electron micrographs of planar–tubular 2D crystals of CitS (type A, grown in acetate buffer) at different magnifications. Negative staining was performed with 2% uranyl acetate. (d) The computed power spectrum of one single cryo-EM image of one CitS 2D crystal, shown here as IQ plot.[47] The lattice vectors are indicated as H and K. Resolution rings are 36, 24 18, 12, and 7 Å.

Table 1. Summary of tested 2D crystallization conditions for CitS

Parameter	Range tested	Best condition
pH	4–9	4.5
Protein concentration (mg/ml)	0.2–2	1.4
Lipid	*E. coli* polar lipid, POPC, POPE, DMPC, DOPC, DOPG, POPS, POPA	POPE:POPC (7:3 and 3:7)
LPR (w/w)	0.1–1.5	0.32–0.35
Detergent	DDM, DM	DM (0.2%)
Temperature (°C)	4–40	32–34
Crystallization technique	Dialysis, Biobeads	Dialysis
Buffer (for pH 4.5)	Citrate, acetate	Acetate
NaCl (mM)	25–600	500
$MgCl_2$ (mM)	0–50	15
KCl (mM)	0–200	0
Glycerol (%) (v/v)	0–20	0
DTT (mM)	0–5	2

DDM, *n*-dodecyl-β-D-maltoside; POPC, 1-palmitoyl-2-oleoyl-sn-glycero-3-phosphocholine; POPE, 1-palmitoyl-2-oleoyl-sn-glycero-3-phosphoethanolamine; DMPC, 1,2-dimyristoyl-sn-glycero-3-phosphocholine; DOPC, 1,2-dioleoyl-sn-glycero-3-phosphocholine; DOPG, 1,2-dioleoyl-sn-glycero-3-phospho-(1'-rac-glycerol); POPS, 1-palmitoyl-2-oleoyl-sn-glycero-3-phospho-L-serine; POPA, 1-palmitoyl-2-oleoyl-sn-glycero-3-phosphate.

range, which might be due to protrusions in the molecule, as found by Moscicka *et al.*[38] Interestingly, crystals grown in acetate buffer were consistently better ordered compared to crystals in citrate buffer with otherwise identical conditions. This might be related to a higher conformational flexibility of CitS in the presence of its substrate citrate as predicted from the model of "alternating access".[7,46,48] In acetate and saturating amounts of Na^+, the transporter might be in a locked and inactive conformation, which benefits crystallization.

For high-resolution data collection, the crystals were plunge frozen in liquid ethane without the addition of common cryo-protectants such as trehalose, glucose, or tannic acid. Other freezing techniques[49] did not yield high-resolution information. Image processing produced two lattices as a result of the two layers formed by the flattened tubes, which were processed independently. A summary of the crystallographic data can be found in Table 2. The unit cell dimensions for type A crystals (in acetate buffer) were 96.0 Å × 106.0 Å with an included angle of 90.0°. The symmetry assignment was $p22_12_1$. Type A crystals yielded structure factor phases up to a resolution of 4.5 Å. We merged data from five micrographs and limited the resulting map to 6 Å resolution, up to where phase residual values were below 37° (see Fig. 2d and Table 2). For the crystals of type B (in citrate buffer), we found unit cell dimensions of 70.9 Å × 68.6 Å with an included angle of 94.3° and *p*2 symmetry assignment. For this crystal form, only one micrograph could be processed to 9 Å resolution.

Table 2. Electron crystallographic data and statistics

	Crystal type	
	Type A (in acetate)	Type B (in citrate)
Plane group symmetry	$p22_12_1$	*p*2
Unit cell dimensions		
a (Å)	96.0	70.9
b (Å)	106.0	68.6
γ (°)	90	94.3
Number of processed images	5	1
Number of unique reflections (IQ ≤ 4) in resolution range	∞–9.5 Å → 350 9.5–6.7 Å → 161 6.7–5.5 Å → 39 ∑ reflections = 550	∞–18 Å → 26 18–12 Å → 36 12–9 Å → 32 ∑ reflections = 94
IQ-weighted phase residuals in resolution range	∞–9.5 Å → 25.0° 9.5–6.7 Å → 34.6° 6.7–5.5 Å → 36.8°	∞–18 Å → 23° 18–12 Å → 29.6° 12–9 Å → 35.4°

Projection structure

Figure 3 illustrates the resulting projection structure (Fig. 3a) and contour plot (Fig. 3b) of CitS at 6 Å resolution in acetate buffer (type A crystals). The crystallographic unit cell accommodates two elliptical shaped molecules with dimensions of 5.2 nm (short axis, *a*) × 9.6 nm (long axis, *b*). The same overall shape and dimensions for CitS can also be found in citrate buffer, where the unit cell is formed by one molecule (type B crystals, Fig. 3c). The observed elliptical shape of the asymmetric unit is consistent with the low-resolution projection structure derived from single-particle analysis of detergent-solubilized dimeric CitS.[38] As expected, the crystal projection map shows a remarkably smaller outer dimension of the molecule (9.6 nm × 5.2 nm) than seen for the detergent-surrounded particles previously observed (16 nm × 8.4 nm).[38] The obtained dimensions of the dimeric CitS symporter are similar to those of other secondary transporters such as the bacterial chloride channel ClC[51] or the Na^+/H^+ exchangers NhaA[52] and NhAP1.[50]

The 2D crystal arrangement shows CitS in a dimeric form, which corroborates the dimerization findings from Blue Native PAGE, single-particle electron microscopy (EM), and fluorescence spectroscopy.[38,39] However, it is still unclear whether the monomeric or the dimeric CitS forms the functional unit. In comparison, most available structures from secondary transporters so far exhibit higher oligomeric states such as dimers (e.g., NhaP1) and trimers (e.g., the H^+/galactose symporter GalP). In those cases, the protomer constitutes the functional unit and oligomerization may predominantly enhance structural stability.[7] An exception is

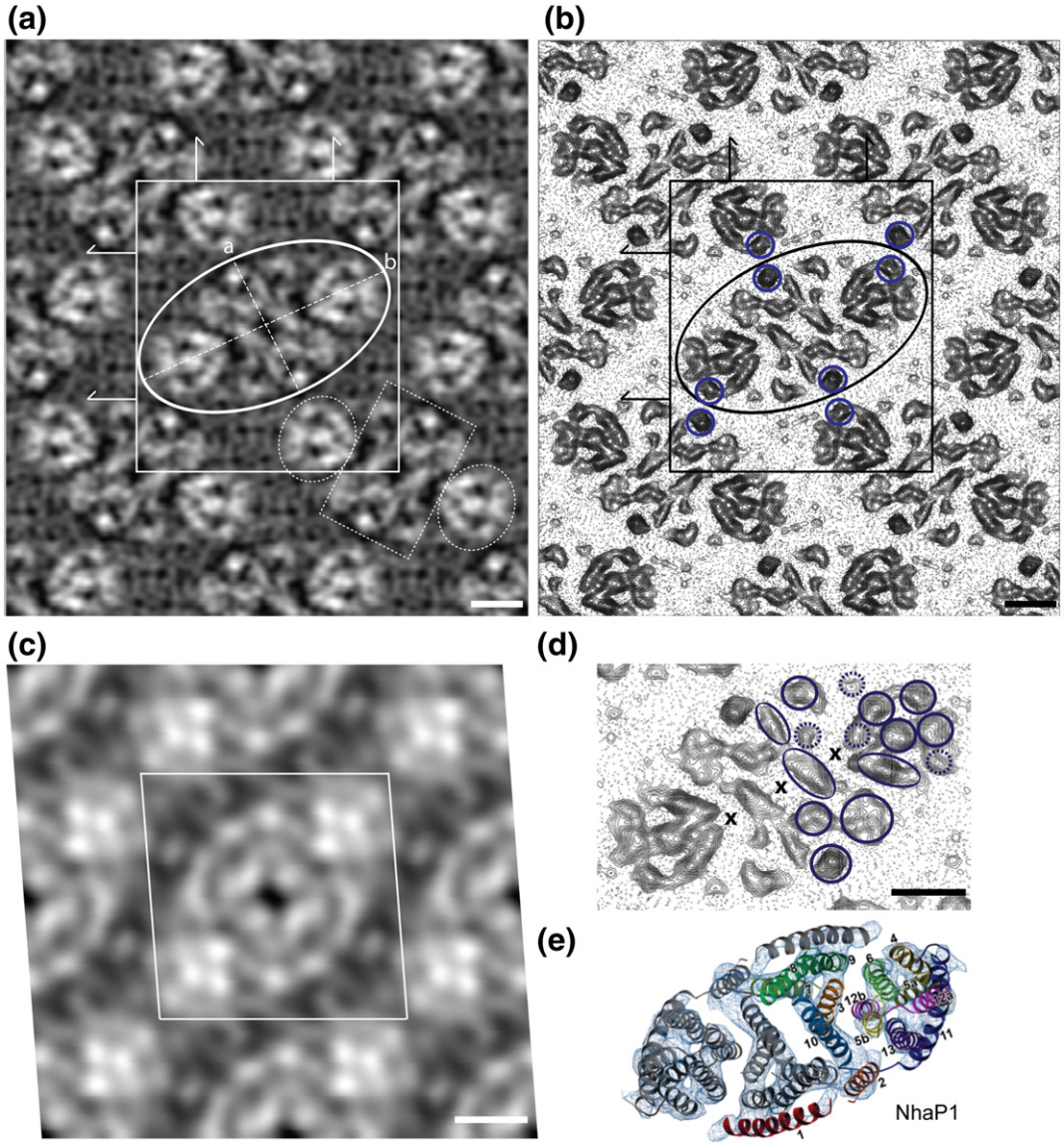

Fig. 3. Projection structure and contour plot of CitS from type A crystals. (a) The merged projection map of CitS from type A crystals at 6 Å resolution. Each unit cell (96.0 Å × 106.0 Å and $\gamma = 90°$) contains two CitS dimers. The screw axes of the $p22_12_1$ plane group are marked by arrows and indicate alternating up and down orientation of adjacent dimers relative to the membrane plane. One CitS dimer is highlighted by a white ellipsis with axes of $a = 5.2$ nm and $b = 9.6$ nm. In the dimer in the lower right corner, three characteristic structural areas are highlighted by dashed white circles and one rectangle. High and low electron densities are depicted in white and black, respectively. No temperature factor was applied. The scale bar represents 2 nm. (b) Contour plot of the map in (a). One CitS dimer is highlighted by a black ellipsis. Blue circles indicate putative electron densities involved in crystal contacts. The scale bar represents 2 nm. (c) Contour plot of CitS from type B crystals at 9 Å resolution. The unit cell (70.9 Å × 68.6 Å and $\gamma = 94.3°$) with applied $p2$ symmetry is marked by a white rhomboid and contains one CitS dimer. No temperature factor was applied. The scale bar represents 2 nm. (d) Contour plot of one CitS dimer at 6 Å resolution. Prominent electron densities in one hypothetical monomer are marked by blue circles. Black crosses indicate regions of low density. The scale bar represents 2 nm. (e) Model of NhaP1 viewed from top. Arabic numbers refer to the 13 helices in the monomer. Corresponding helices in the two domains are in the same color. Reproduced from Ref. [50] with kind permission.

BetP, where trimerization was found to be important for function and regulation.[53]

The projection map of the dimeric CitS shows a circularly arranged group of electron-dense regions at both ends of the long axis, while the central part of dimeric CitS is formed by a more rectangular arrangement. These clusters are separated by areas of low density. Surprisingly, a similar global architecture was previously found for the bacterial sodium/proton antiporter NhaP1, which exhibits 13

transmembrane α-helices organized in two homologue domains connected by helix 7 (Fig. 3e, reproduced from Goswami *et al.*[50]).

The projection map of the putative CitS dimer (Fig. 3d) with an assumed monomer–monomer interface formed by the short axis allows the identification of 11 stronger (blue circles) and 4 weaker densities (dashed blue circles) for each monomer. The stronger densities likely correspond to projections of α-helical TMSs. Two of them (blue circles in Fig. 3b) are strongly contrasted and of limited extension, suggesting them to be in nearly perpendicular orientation relative to the membrane plane. These seem to be involved in defining the crystal contacts between adjacent dimers (Fig. 3b). The number of strong densities in the CitS projection map is in agreement with the current model, predicting 11 membrane-spanning α-helices (Fig. 1a).[36] The elongation of most TMS densities suggests those to be slightly tilted in the membrane plane, in line with other secondary transporters of known structure such as Glt_{Ph}[13] or LeuT.[14]

Monomer–monomer interface, N- and C- terminal domain arrangement

According to cross-linking studies of biotin affinity domain-tagged CitS, the monomer–monomer interface of CitS was proposed to be located at the short axis of the elliptical dimer.[40] Potential models that fulfill this criterion are presented in Fig. 4a and b. Both interfaces differ only in the monomer affiliation of the prominent perpendicular helix at both ends of the putative interfaces. Figure 4c and d present two alternative hypothetical interface locations. However, only the models in Fig. 4a and b are compatible with interfaces found in other dimeric secondary transporters such as NhaP1[54] and ClC.[12] The precise localization of the dimer interface will have to await the availability of a higher-resolution 3D structure.

Possible arrangements of the N- and C-terminal five-helix domains within each CitS monomer are indicated in Fig. 4e–g. Krupnik *et al.*[40] argued that (1) the N-terminus of CitS might be located at the end of the short axis, and (2) the large cytoplasmic loop might be at the tip of the dimer's long axis. We also note that (3) an internal symmetry can roughly be discerned in the projection map of each CitS monomer along the long axis of the dimer, likely originating from a similar fold of the N- and C-terminal domains of CitS. Finally, (4) Dobrowolski *et al.*[43] assigned the substrate translocation site to the interface of both domains, formed by helices 5/6 and 10/11 with the associated reentrant loops. Based on these four assumptions, we propose three different feasible models for the assignment of N- and C-terminal halves of each monomer (Fig. 4e–g). In all models, the prominent perpendicular α-helix at the assumed protomer interface is defined as the N-terminal helix 1 (yellow, compare Fig. 1a). Adjacent to this, we defined five helices as N-domain (blue) and C-domain (red). Models 1 and 2 differ in the position of the interface between two monomers, which leads to an altered position of helix 1, and with it, a flipping of the two

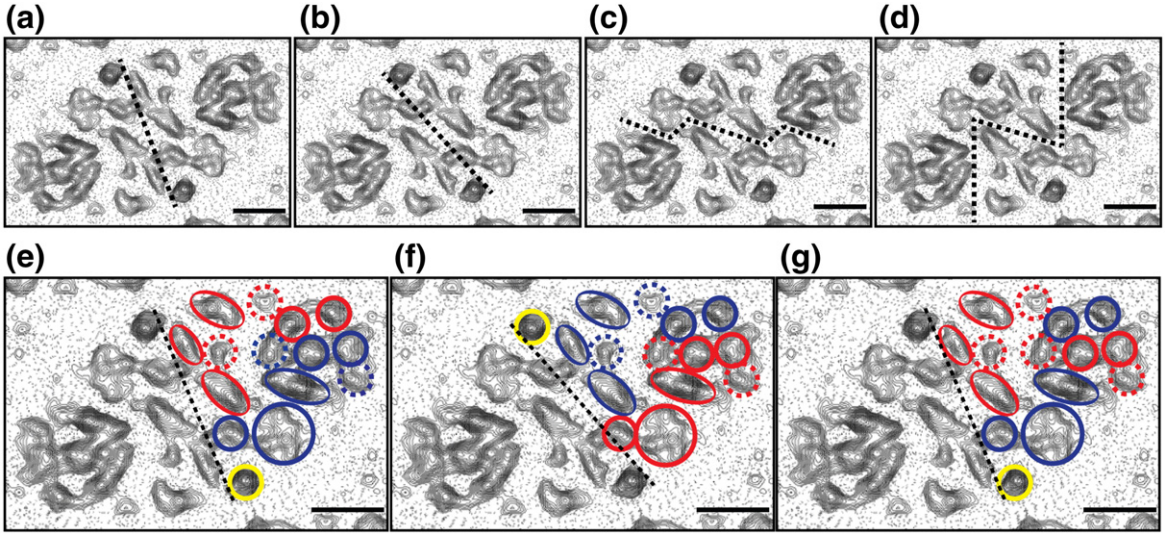

Fig. 4. Possible monomer–monomer interfaces and domain orientations in the CitS dimer. Each panel shows one CitS dimer projection contour plot at 6 Å resolution. (a–d) Hypothetical dimer interfaces are marked by black broken lines. (e–g) Models of domain organization. The N-terminal helix (yellow) sits at the end of the short axis. The N-domain is highlighted in blue, while helices belonging to the C-domain are depicted in red. The scale bars represent 2 nm.

domains. In both models, the two domains appear as structurally independent from each other with only little helix intertwining. Similar domain organizations (in terms of limited domain intertwining) were previously found for secondary transporters of the major facilitator family, for example, LacY, GlpT, and EmrD.[7] In a third model (Fig. 4g), we flipped the four helices found in the cluster at the tip of the dimer, which would lead to a higher degree of helix intertwining between the N- and C-terminal domains. Here, CitS would rather resemble secondary transporters of the LeuT fold (e.g., LeuT, BetP, and CaiT) and, again, NhAP1. For all three models, an approximate internal symmetry can be applied on the N- and C-terminal domains by rotating one of the domains by 180° in the membrane plane around the long axis of the dimer. This symmetry does not apply for the single N-terminal helix I, which speaks for a valid assignment of that yellow density in Fig. 4e–g as helix I. However, compared to other secondary transporters, the internal symmetry we find in our models is rather weak, especially in the central part of the molecule. This might reflect a distinct conformation of CitS as it is trapped in the presented crystals. On the other hand, the weak internal symmetry could also be a structural feature of CitS and other members of the ST[3] class.

According to functional studies by Dobrowolski and Lolkema,[42] the helical TMSs 5/6 and 10/11 and the reentrant loops Va and Xb are involved in substrate translocation. In addition, the translocation site might be relatively distant from the dimer interface, as it is also found for most other secondary transporters.[7,46,48] Based on these findings, a possible substrate translocation site in CitS could be formed by the circular helix cluster at each tip of the dimeric molecule. However, a high-resolution 3D map of CitS is needed to clearly assign the helix model and translocation site.

Conclusion

In this study, we present the first sub-nanometer projection map of the secondary citrate/Na^+ symporter CitS as a representative member of the 2-HCT family. The projection structure at 6 Å resolution exhibits at least 11 densities to which α-helical TMSs can be assigned. These are organized in three major clusters in the dimeric molecule. The CitS projection map shows a high level of similarity to that of the unrelated Na^+/H^+ antiporter NhaP1. We propose a hypothetical model for the monomer–monomer interface in the CitS dimer and discuss possible orientations of the two N- and C-terminal sub-domains of CitS. According to these models, helix I would be located at the end of the short axis of the elliptical dimer. The N- and C-terminal domains would exhibit an approximate internal symmetry, which can be recognized in the approximate mirror symmetry along the long axis of the molecule. We speculate the substrate translocation site to be formed by at least four helices at the distant tip of each monomeric molecule.

Materials and Methods

Protein expression and purification

CitS was expressed and purified to homogeneity as described before[55,56] with modifications. Briefly, the N-terminally His-tagged CitS was overexpressed in *E. coli* C43(DE3) by fermentation. Purification was performed by membrane solubilization in *n*-dodecyl-β-D-maltoside and immobilized metal-ion affinity chromatography (Ni^{2+}-NTA, Quiagen). Detergent exchange to *n*-decyl-β-D-maltoside (DM) was performed during immobilized metal-ion affinity chromatography. The protein was further polished by passing over a size-exclusion chromatography column (Superdex 200 10/300 GL, GE Healthcare) and concentrated with microcon (Amicon), with a molecular mass cutoff of 100 kDa.

2D crystallization

2D crystals of CitS were grown by microdialysis in 70-μl buttons sealed with a membrane with a molecular mass cutoff of 14 kDa. Lipids solubilized in 2% DM were added to the membrane protein solution (1.4 mg/ml in 0.2% DM) and incubated on ice overnight. Seventy microliters of this ternary mixture was dialyzed against 2 L of buffer containing 20 mM sodium acetate, pH 4.5, 500 mM NaCl, 15 mM $MgCl_2$, 2 mM DTT, and 2 mM NaN_3 at temperatures of 32 °C (2 days) and 34 °C (3 days). The quality of the harvested 2D crystals was evaluated by negative-stain EM. This was done by adsorbing 3 μl of crystal solution to 200-mesh carbon-coated copper grids that were rendered hydrophilic by glow-discharging in air for 20 s. Grids were washed in double-distilled water and stained with 2% uranyl acetate. Pictures were taken on a Philips CM10 equipped with a LaB_6 filament and operated at an accelerating voltage of 80 kV.

EM and image processing

For cryo-EM, crystal solution on glow-discharged carbon-coated holey carbon grids (Quantifoil R2/2, Quantifoil Micro Tools, Jena, Germany) was blotted and rapidly plunge frozen in liquid-nitrogen-cooled liquid ethane, using a MarkII Vitrobot (FEI, Eindhoven, Netherlands). The frozen grids were transferred to a Gatan-626 cryo-holder and analyzed in a Philips CM200 transmission electron microscope, equipped with a field-emission gun and operated at 200 kV. Pictures were taken at a nominal magnification of 50,000× using low-dose imaging techniques with an electron dose of approximately 5 $e^-/Å^2$

and defocus values ranging from 0.5 to 0.9 μm. Images were recorded on Kodak SO-163 film, which was developed for 7 min in full-strength Kodak D19 developer solution. Image quality was assessed by optical diffraction on a home-built laser diffractometer. The best images were digitized using a Heidelberg Primescan D 7100 scanner with a step size of 1 Å/pixel at the specimen level. Digital images were processed using the 2dx software suite,[57,58] which is based on the MRC programs.[59] Images were corrected for crystal disorders by three rounds of unbending. This was followed by a correction for the contrast transfer function and astigmatism. Symmetry was determined using the allspace program[60] within 2dx.

Acknowledgements

We thank Mohamed Chami for support for cryo-EM. We also thank Werner Kühlbrandt for permission to reproduce the NhaP1 map in Fig. 3d. This work was was supported by the Swiss National Science Foundation in the framework of the National Center of Competence in Research, Structural Biology, and in the Swiss Initiative for Systems Biology (SystemsX.ch).

Author Contributions. F.K. and M.K. contributed equally to this work. M.K. expressed and purified the protein. F.K. performed 2D crystallization and EM. H.S. and F.K. carried out image processing. All authors interpreted the results and wrote the manuscript.

References

1. Saier, M. H., Jr (2000). A functional–phylogenetic classification system for transmembrane solute transporters. *Microbiol. Mol. Biol. Rev.* **64**, 354–411.
2. Busch, W. & Saier, M. H., Jr (2004). The IUBMB-endorsed transporter classification system. *Mol. Biotechnol.* **27**, 253–262.
3. Paulsen, I. T., Sliwinski, M. K. & Saier, M. H., Jr (1998). Microbial genome analyses: global comparisons of transport capabilities based on phylogenies, bioenergetics and substrate specificities. *J. Mol. Biol.* **277**, 573–592.
4. Lolkema, J. S. & Slotboom, D. J. (1998). Estimation of structural similarity of membrane proteins by hydropathy profile alignment. *Mol. Membr. Biol.* **15**, 33–42.
5. Lolkema, J. S. & Slotboom, D. J. (2003). Classification of 29 families of secondary transport proteins into a single structural class using hydropathy profile analysis. *J. Mol. Biol.* **327**, 901–909.
6. Ter Horst, R. & Lolkema, J. S. (2012). Membrane topology screen of secondary transport proteins in structural class ST[3] of the MemGen classification. Confirmation and structural diversity. *Biochim. Biophys. Acta*, **1818**, 72–81.
7. Forrest, L. R., Krämer, R. & Ziegler, C. (2011). The structural basis of secondary active transport mechanisms. *Biochim. Biophys. Acta*, **1807**, 167–188.
8. Murakami, S., Nakashima, R., Yamashita, E. & Yamaguchi, A. (2002). Crystal structure of bacterial multidrug efflux transporter AcrB. *Nature*, **419**, 587–593.
9. Abramson, J., Smirnova, I., Kasho, V., Verner, G., Kaback, H. R. & Iwata, S. (2003). Structure and mechanism of the lactose permease of *Escherichia coli*. *Science*, **301**, 610–615.
10. Huang, Y., Lemieux, M. J., Song, J., Auer, M. & Wang, D. N. (2003). Structure and mechanism of the glycerol-3-phosphate transporter from *Escherichia coli*. *Science*, **301**, 616–620.
11. Hunte, C., Screpanti, E., Venturi, M., Rimon, A., Padan, E. & Michel, H. (2005). Structure of a Na^+/H^+ antiporter and insights into mechanism of action and regulation by pH. *Nature*, **435**, 1197–1202.
12. Dutzler, R., Campbell, E. B., Cadene, M., Chait, B. T. & MacKinnon, R. (2002). X-ray structure of a ClC chloride channel at 3.0 Å reveals the molecular basis of anion selectivity. *Nature*, **415**, 287–294.
13. Yernool, D., Boudker, O., Jin, Y. & Gouaux, E. (2004). Structure of a glutamate transporter homologue from *Pyrococcus horikoshii*. *Nature*, **431**, 811–818.
14. Yamashita, A., Singh, S. K., Kawate, T., Jin, Y. & Gouaux, E. (2005). Crystal structure of a bacterial homologue of Na^+/Cl-dependent neurotransmitter transporters. *Nature*, **437**, 215–223.
15. Pebay-Peyroula, E., Dahout-Gonzalez, C., Kahn, R., Trezeguet, V., Lauquin, G. J. & Brandolin, G. (2003). Structure of mitochondrial ADP/ATP carrier in complex with carboxyatractyloside. *Nature*, **426**, 39–44.
16. Faham, S., Watanabe, A., Besserer, G. M., Cascio, D., Specht, A., Hirayama, B. A. *et al.* (2008). The crystal structure of a sodium galactose transporter reveals mechanistic insights into Na^+/sugar symport. *Science*, **321**, 810–814.
17. Berardi, M. J., Shih, W. M., Harrison, S. C. & Chou, J. J. (2011). Mitochondrial uncoupling protein 2 structure determined by NMR molecular fragment searching. *Nature*, **476**, 109–113.
18. Yin, Y., He, X., Szewczyk, P., Nguyen, T. & Chang, G. (2006). Structure of the multidrug transporter EmrD from *Escherichia coli*. *Science*, **312**, 741–744.
19. Ubarretxena-Belandia, I., Baldwin, J. M., Schuldiner, S. & Tate, C. G. (2003). Three-dimensional structure of the bacterial multidrug transporter EmrE shows it is an asymmetric homodimer. *EMBO J.* **22**, 6175–6181.
20. Tate, C. G. (2006). Comparison of three structures of the multidrug transporter EmrE. *Curr. Opin. Struct. Biol.* **16**, 457–464.
21. Chen, Y. J., Pornillos, O., Lieu, S., Ma, C., Chen, A. P. & Chang, G. (2007). X-ray structure of EmrE supports dual topology model. *Proc. Natl Acad. Sci. USA*, **104**, 18999–19004.
22. Korkhov, V. M. & Tate, C. G. (2009). An emerging consensus for the structure of EmrE. *Acta Crystallogr., Sect. D: Biol. Crystallogr.* **65**, 186–192.
23. Dang, S., Sun, L., Huang, Y., Lu, F., Liu, Y., Gong, H. *et al.* (2010). Structure of a fucose transporter in an outward-open conformation. *Nature*, **467**, 734–738.

24. Weyand, S., Shimamura, T., Yajima, S., Suzuki, S., Mirza, O., Krusong, K. *et al.* (2008). Structure and molecular mechanism of a nucleobase-cation-symport-1 family transporter. *Science*, **322**, 709–713.
25. Ressl, S., Terwisscha van Scheltinga, A. C., Vonrhein, C., Ott, V. & Ziegler, C. (2009). Molecular basis of transport and regulation in the Na(+)/betaine symporter BetP. *Nature*, **458**, 47–52.
26. Fang, Y., Jayaram, H., Shane, T., Kolmakova-Partensky, L., Wu, F., Williams, C. *et al.* (2009). Structure of a prokaryotic virtual proton pump at 3.2 Å resolution. *Nature*, **460**, 1040–1043.
27. Shaffer, P. L., Goehring, A., Shankaranarayanan, A. & Gouaux, E. (2009). Structure and mechanism of a Na^+-independent amino acid transporter. *Science*, **325**, 1010–1014.
28. Schulze, S., Köster, S., Geldmacher, U., Terwisscha van Scheltinga, A. C. & Kühlbrandt, W. (2010). Structural basis of Na(+)-independent and cooperative substrate/product antiport in CaiT. *Nature*, **467**, 233–236.
29. Newstead, S., Drew, D., Cameron, A. D., Postis, V. L., Xia, X., Fowler, P. W. *et al.* (2011). Crystal structure of a prokaryotic homologue of the mammalian oligopeptide-proton symporters, PepT1 and PepT2. *EMBO J.* **30**, 417–426.
30. Lu, F., Li, S., Jiang, Y., Jiang, J., Fan, H., Lu, G. *et al.* (2011). Structure and mechanism of the uracil transporter UraA. *Nature*, **472**, 243–246.
31. Hu, N. J., Iwata, S., Cameron, A. D. & Drew, D. (2011). Crystal structure of a bacterial homologue of the bile acid sodium symporter ASBT. *Nature*, **478**, 408–411.
32. Sobczak, I. & Lolkema, J. S. (2005). Structural and mechanistic diversity of secondary transporters. *Curr. Opin. Microbiol.* **8**, 161–167.
33. Bandell, M., Ansanay, V., Rachidi, N., Dequin, S. & Lolkema, J. S. (1997). Membrane potential-generating malate (MleP) and citrate (CitP) transporters of lactic acid bacteria are homologous proteins. Substrate specificity of the 2-hydroxycarboxylate transporter family. *J. Biol. Chem.* **272**, 18140–18146.
34. Lolkema, J. S. (2006). Domain structure and pore loops in the 2-hydroxycarboxylate transporter family. *J. Mol. Microbiol. Biotechnol.* **11**, 318–325.
35. Lolkema, J. S., Sobczak, I. & Slotboom, D. J. (2005). Secondary transporters of the 2HCT family contain two homologous domains with inverted membrane topology and trans re-entrant loops. *FEBS J.* **272**, 2334–2344.
36. van Geest, M. & Lolkema, J. S. (2000). Membrane topology of the Na(+)/citrate transporter CitS of *Klebsiella pneumoniae* by insertion mutagenesis. *Biochim. Biophys. Acta*, **1466**, 328–338.
37. Sobczak, I. & Lolkema, J. S. (2005). Loop VIII/IX of the Na^+-citrate transporter CitS of *Klebsiella pneumoniae* folds into an amphipathic surface helix. *Biochemistry*, **44**, 5461–5470.
38. Moscicka, K. B., Krupnik, T., Boekema, E. J. & Lolkema, J. S. (2009). Projection structure by single-particle electron microscopy of secondary transport proteins GltT, CitS, and GltS. *Biochemistry*, **48**, 6618–6623.
39. Kästner, C. N., Prummer, M., Sick, B., Renn, A., Wild, U. P. & Dimroth, P. (2003). The citrate carrier CitS probed by single-molecule fluorescence spectroscopy. *Biophys. J.* **84**, 1651–1659.
40. Krupnik, T., Dobrowolski, A. & Lolkema, J. S. (2011). Cross-linking of dimeric CitS and GltS transport proteins. *Mol. Membr. Biol.* **28**, 243–253.
41. Sobczak, I. & Lolkema, J. S. (2004). Alternating access and a pore-loop structure in the Na^+-citrate transporter CitS of *Klebsiella pneumoniae*. *J. Biol. Chem.* **279**, 31113–31120.
42. Dobrowolski, A. & Lolkema, J. S. (2009). Functional importance of GGXG sequence motifs in putative reentrant loops of 2HCT and ESS transport proteins. *Biochemistry*, **48**, 7448–7456.
43. Dobrowolski, A., Fusetti, F. & Lolkema, J. S. (2010). Cross-linking of trans reentrant loops in the Na(+)-citrate transporter CitS of *Klebsiella pneumoniae*. *Biochemistry*, **49**, 4509–4515.
44. Lolkema, J. S., Enequist, H. & van der Rest, M. E. (1994). Transport of citrate catalyzed by the sodium-dependent citrate carrier of *Klebsiella pneumoniae* is obligatorily coupled to the transport of two sodium ions. *Eur. J. Biochem.* **220**, 469–475.
45. Pos, K. M. & Dimroth, P. (1996). Functional properties of the purified Na(+)-dependent citrate carrier of *Klebsiella pneumoniae*: evidence for asymmetric orientation of the carrier protein in proteoliposomes. *Biochemistry*, **35**, 1018–1026.
46. Krishnamurthy, H., Piscitelli, C. L. & Gouaux, E. (2009). Unlocking the molecular secrets of sodium-coupled transporters. *Nature*, **459**, 347–355.
47. Henderson, R., Baldwin, J. M., Ceska, T. A., Zemlin, F., Beckmann, E. & Downing, K. H. (1990). Model for the structure of bacteriorhodopsin based on high-resolution electron cryo-microscopy. *J. Mol. Biol.* **213**, 899–929.
48. Abramson, J. & Wright, E. M. (2009). Structure and function of Na(+)-symporters with inverted repeats. *Curr. Opin. Struct. Biol.* **19**, 425–432.
49. Gyobu, N., Tani, K., Hiroaki, Y., Kamegawa, A., Mitsuoka, K. & Fujiyoshi, Y. (2004). Improved specimen preparation for cryo-electron microscopy using a symmetric carbon sandwich technique. *J. Struct. Biol.* **146**, 325–333.
50. Goswami, P., Paulino, C., Hizlan, D., Vonck, J., Yildiz, O. & Kühlbrandt, W. (2011). Structure of the archaeal Na^+/H^+ antiporter NhaP1 and functional role of transmembrane helix 1. *EMBO J.* **30**, 439–449.
51. Mindell, J. A., Maduke, M., Miller, C. & Grigorieff, N. (2001). Projection structure of a ClC-type chloride channel at 6.5 Å resolution. *Nature*, **409**, 219–223.
52. Appel, M., Hizlan, D., Vinothkumar, K. R., Ziegler, C. & Kühlbrandt, W. (2009). Conformations of NhaA, the Na^+/H^+ exchanger from *Escherichia coli*, in the pH-activated and ion-translocating states. *J. Mol. Biol.* **388**, 659–672.
53. Perez, C., Khafizov, K., Forrest, L. R., Krämer, R. & Ziegler, C. (2011). The role of trimerization in the osmoregulated betaine transporter BetP. *EMBO Rep.* **12**, 804–810.
54. Vinothkumar, K. R., Smits, S. H. & Kühlbrandt, W. (2005). pH-induced structural change in a sodium/proton antiporter from *Methanococcus jannaschii*. *EMBO J.* **24**, 2720–2729.
55. Huber, T., Steiner, D., Röthlisberger, D. & Plückthun, A. (2007). In vitro selection and characterization of DARPins and Fab fragments for the co-crystallization

of membrane proteins: the Na(+)-citrate symporter CitS as an example. *J. Struct. Biol.* **159**, 206–221.
56. Kästner, C. N., Dimroth, P. & Pos, K. M. (2000). The Na^+-dependent citrate carrier of *Klebsiella pneumoniae*: high-level expression and site-directed mutagenesis of asparagine-185 and glutamate-194. *Arch. Microbiol.* **174**, 67–73.
57. Gipson, B., Zeng, X. & Stahlberg, H. (2008). 2dx—Automated 3D structure reconstruction from 2D crystal data. *Microsc. Microanal.* **14**, 1290–1291.
58. Gipson, B., Zeng, X., Zhang, Z. & Stahlberg, H. (2007). 2dx—User-friendly image processing for 2D crystals. *J. Struct. Biol.* **157**, 64–72.
59. Crowther, R. A., Henderson, R. & Smith, J. M. (1996). MRC image processing programs. *J. Struct. Biol.* **116**, 9–16.
60. Valpuesta, J. M., Carrascosa, J. L. & Henderson, R. (1994). Analysis of electron microscope images and electron diffraction patterns of thin crystals of phi 29 connectors in ice. *J. Mol. Biol.* **240**, 281–287.